

Conditions for convective deep inflow

Yi-Hung Kuo¹ and J. David Neelin²

¹University of California, Los Angeles

²University of California Los Angeles

November 23, 2022

Abstract

Observations and cloud-resolving simulations suggest that a convective updraft structure drawing mass from a deep lower-tropospheric layer occurs over a wide range of conditions. This occurs for both mesoscale convective systems (MCSs) and less-organized convection, raising the question: Is there a simple, universal characteristic governing the deep inflow? Here we argue that nonlocal dynamics of the response to buoyancy are key. For precipitating deep-convective features including horizontal scales comparable to a substantial fraction of the troposphere depth, the response to buoyancy tends to yield deep inflow into the updraft mass flux. Precipitation features in this range of scales are found to dominate contributions to observed convective precipitation for both MCS and less-organized convection. The importance of such nonlocal dynamics implies thinking beyond parcel models with small-scale turbulence for representation of convection in climate models. Solutions here lend support to investment in parameterizations at a complexity between conventional and superparameterization.

Conditions for convective deep inflow

Yi-Hung Kuo & J. David Neelin

Department of Atmospheric and Oceanic Sciences, University of California, Los Angeles, CA 90095

Key Points:

- Observations and simulations point to a common structure of convective mass flux drawing air from a deep layer in the lower troposphere
- Most deep-convective precipitation comes from features with horizontal size comparable to or exceeding the lower tropospheric depth
- For these, the nonlocal response of convective updrafts to buoyancy provides a simple explanation for the observed deep-inflow structure

Corresponding author: Yi-Hung Kuo, yhkuo@atmos.ucla.edu

Abstract

Observations and cloud-resolving simulations suggest that a convective updraft structure drawing mass from a deep lower-tropospheric layer occurs over a wide range of conditions. This occurs for both mesoscale convective systems (MCSs) and less-organized convection, raising the question: Is there a simple, universal characteristic governing the deep inflow? Here we argue that nonlocal dynamics of the response to buoyancy are key. For precipitating deep-convective features including horizontal scales comparable to a substantial fraction of the troposphere depth, the response to buoyancy tends to yield deep inflow into the updraft mass flux. Precipitation features in this range of scales are found to dominate contributions to observed convective precipitation for both MCS and less-organized convection. The importance of such nonlocal dynamics implies thinking beyond parcel models with small-scale turbulence for representation of convection in climate models. Solutions here lend support to investment in parameterizations at a complexity between conventional and superparameterization.

Plain Language Summary

Deep convection, whether in isolated thunderstorms or organized mesoscale convective systems, is a leading effect in climate dynamics and climate change, yet it remains subject to large uncertainties in climate models. The way that air enters convective clouds plays a substantial role in this uncertainty, and recently the importance of inflow through a deep layer in the lower troposphere has been noted, although why this should apply for both isolated and organized convection has been unclear. Here we show that an aspect of dynamics omitted from conventional climate model representations provides a simple explanation for this for large clouds that account for most convective precipitation. This suggests physical effects requiring substantial revisions in climate models.

1 Introduction

Accurate simulation and forecasting of weather and climate depends on adequate representations of deep convection in general circulation models (GCMs). This remains a challenging subject (Randall et al., 2003; Kuo et al., 2020; Leung et al., 2022) even with the advances in cloud-resolving models (CRMs) and machine learning (Wing et al., 2020; Bretherton et al., 2021). Challenges arise especially in regards to (i) organized convection, such as mesoscale convective systems (MCSs) (Moncrieff et al., 2012; Yano & Moncrieff, 2016) that account for a significant fraction of precipitation (Nesbitt et al., 2006); and (ii) the entrainment process of environmental air entering in-cloud updrafts (Plant, 2010; Sherwood et al., 2014). The traditional view of entrainment assumes a plume/parcel rising from near the surface that is modified by its immediate surroundings via localized, small-scale turbulent mixing (Arakawa & Schubert, 1974). This motivated efforts to quantify a postulated local entrainment rate (Siebesma et al., 2003; Del Genio & Wu, 2010; Masunaga & Luo, 2016)—primarily by indirect means—from which mass flux can be derived for plume models in parameterization schemes (de Rooy & Siebesma, 2010; Morrison, 2017). At odds with the above conceptual model, a range of turbulent scales contributes to the mixing within actual convective entities, and features of larger scales are instrumental for nonlocal transport by convection (Siebesma et al., 2007).

Field measurements of convective updrafts during aircraft campaigns (LeMone & Zipser, 1980; Lucas et al., 1994) and by radar wind profilers (Schiro et al., 2018; Savazzi et al., 2021), in accordance with CRM simulations (Robe & Emanuel, 1996; Li et al., 2008), identify a common mass flux structure that gradually increases throughout the lower troposphere. Contributions to this can occur through coherent inflow (Moncrieff, 1992)—termed dynamic entrainment (Houghton & Cramer, 1951; Ferrier & Houze, 1989)—in contrast with the conventional paradigm of small-scale mixing. Deep-inflow profiles, with environmental air entering the updraft through a deep lower-tropospheric layer, can also

61 be inferred from the dependence of precipitation on the temperature-moisture environ-
 62 nment as a function of lower-tropospheric layer (Ahmed & Neelin, 2018). The deep-inflow
 63 profile is in general agnostic as to whether inflow occurs by spatially coherent flow, small-
 64 scale turbulence, or both.

65 Given the importance of mass flux in convective parameterizations, the occurrence
 66 of simple vertical structures demands explanation, particularly since any potential for
 67 directly constraining such structures could aid in bypassing the elusive task of determin-
 68 ing vertical dependence of entrainment rate (Kuang & Bretherton, 2006; Romps, 2010).
 69 The apparent widespread occurrence of deep-inflow structures, together with the sur-
 70 prising observation that such structures occur similarly for both MCS and less-organized
 71 deep convection (Schiro et al., 2018), raises the question of whether there is some uni-
 72 versal characteristic governing the dynamics of deep inflow.

73 Here we adapt elements from the anelastic modeling literature to show how they
 74 may provide an explanation for this specific physical phenomenon. As prelude, section
 75 2 reviews evidence for deep inflow, previews the potential role of nonlocal solutions, and
 76 provides an observational analysis that indicates the range of horizontal scales in con-
 77 vective precipitation features. We then recap anelastic equations for the response to buoy-
 78 ancy, cast in a form suitable for vertical acceleration (section 3), and show the implica-
 79 tions for vertically nonlocal response for a given wavelength. In section 4, we examine
 80 response to horizontally localized buoyancy features while demonstrating robustness to
 81 smaller scale variations. Finally we discuss the conditions under which the nonlocal so-
 82 lution provides a simple explanation for deep inflow and implications for convective pa-
 83 rameterizations based on parcel models that neglect these effects.

84 2 Convective precipitation feature scales and inflow

85 Fig. 1 provides an overview of key ingredients of the deep-inflow problem and of
 86 the proposed solution. First, Fig. 1a summarizes the observed deep-convective updrafts
 87 in the lower troposphere. The gradual increase of mass flux with height implies horizon-
 88 tal convergence of environmental air into the updraft through much of the lower tropo-
 89 sphere. Such mass flux profiles are characteristic of both MCS and less-organized con-
 90 vection.

91 Second, Fig. 1b provides a thumbnail of key results from the nonlocal response to
 92 buoyancy elaborated in subsequent sections. For localized net-positive buoyancy struc-
 93 tures of horizontal diameter D and vertical extent $4 \leq z \leq 8$ km, the nonlocal response
 94 of mass flux $\partial_t(\rho_0 \bar{w})$ averaged within the diameter yields a deep-inflow profile through
 95 the lower troposphere. This tends to converge to a roughly linear increase for a broad
 96 range of reasonable conditions when D is comparable to the depth of the tropospheric
 97 layer under consideration.

98 Third, in Fig. 1c we quantify the claim that much of the deep-convective precipi-
 99 tation comes from features that include such horizontal scales (Appendix A). Contigu-
 100 ous features of convective precipitation are identified from satellite precipitation radar
 101 (PR) retrievals. The contribution to total convective precipitation is shown as a func-
 102 tion of feature size estimated two different ways: by cord length of the feature and by
 103 square root of the area of the feature. The contribution to convective precipitation is fur-
 104 ther separated by features that meet common criteria for MCS, and less-organized fea-
 105 tures that do not. Note that stratiform precipitation is *not* included, since we wish to
 106 focus on the scales of features of the deep-convective precipitation. For both MCS and
 107 less-organized convection, the precipitation contribution peaks around 15 km, and $> 70\%$
 108 of the total convective rain is from events of this scale or greater for both feature size
 109 measures. That is, convective rain is mostly from deep-convective features whose hor-
 110 izontal extent is comparable to the depth of the troposphere. MCS features tend to have

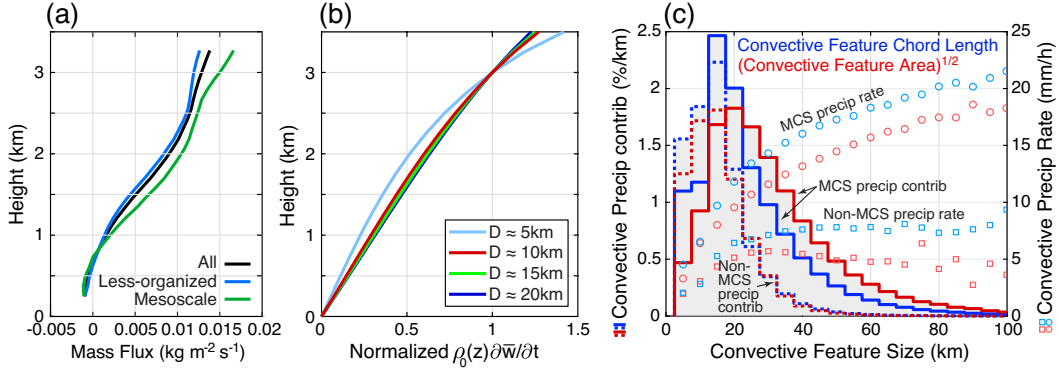


Figure 1. (a) Mean deep-convective updraft mass flux profiles in the lower troposphere for mesoscale, less-organized, and all precipitating convective events estimated from radar wind profiler during the GOAmazon campaign adapted from Schiro et al. (2018). (b) Theoretical response of convective mass flux to buoyancy tartares of vertical extent $4 \leq z \leq 8$ km and varying horizontal diameter D . The tartares consist of randomly-generated small cylindrical bubbles with a 7:3 warm-to-cold bubble ratio (see Fig. 4a). The response profiles are the mean within the diameter D and averaged over an ensemble of 10 tartare realizations, then normalized using values at $z = 3$ km. (c) Convective precipitation contribution (curves) and precipitation rate (markers), for MCS and non-MCS features, conditioned on convective feature size measured by chord length (blue) and square root of area (red). The areas under the MCS and non-MCS precipitation contribution curves sum to unity. Feature size is solely based on contiguous *convective* precipitation pixels.

111 greater contribution to convective rain at large sizes than do less-organized features. While
 112 the conditionally averaged convective precipitation rate for less-organized features (squares)
 113 levels off as size exceeds ~ 25 km, the MCS precipitation rate (circles) continues to in-
 114 crease asymptotically as roughly the $1/4$ -th power of size.

115 The convective precipitation region is not necessarily identical to that of the buoy-
 116 ancy, but provides a rough measure of the existence of strong updrafts and downdrafts
 117 indicative of buoyancy anomalies. The spatiotemporal coverage of the satellite PR
 118 provides regions and periods extensive enough to identify typical characteristics of convec-
 119 tion. We also note that the PR resolution ~ 5 km coarse-grains smaller scale variations,
 120 but suffices to support that localized features containing substantial convective rain oc-
 121 cur over a broad range of scales. The nonlocal effects discussed below also help justify
 122 such coarse-graining.

123 We thus have 1) observational evidence that much of the convective rain in both
 124 MCS and less-organized systems comes from features with characteristic sizes of the con-
 125 vection exceeding ~ 10 km; and 2) a theoretical basis for how the nonlocal nature of the
 126 response to buoyancy tends to yield deep inflow on such scales.

127 3 Nonlocal response to buoyancy

128 We follow the anelastic framework (Ogura & Phillips, 1962) to derive the diagnos-
 129 tic equation for the response to buoyancy. The anelastic approximation assumes a hor-
 130 izontally homogeneous, time-invariant atmospheric density $\rho_0(z)$, allowing the govern-
 131 ing system to filter acoustic waves and retain nonhydrostatic solutions relevant for deep
 132 convection with $O(1)$ aspect ratio (Markowski & Richardson, 2011). Thus the anelas-

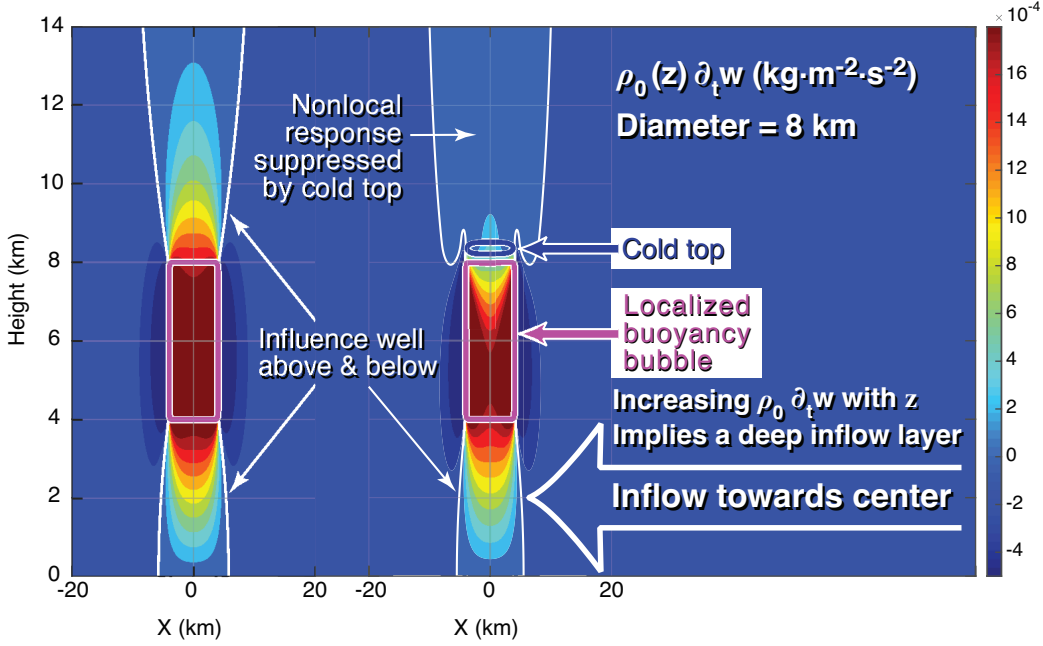


Figure 2. Cross section of vertical mass flux response (color shading; $\text{kg}/\text{m}^2\text{s}^2$) to idealized buoyancy forcing with constant $B = 0.01 \text{ m/s}^2$ in cylindrical bubbles of 8-km diameter (magenta contours). The case on the right also includes a negatively buoyant region immediately above ($B = -0.06 \text{ m/s}^2$) to illustrate the tendency of the “convective cold top” to cancel vertical motion above the main updraft. The white contours indicate zero response. The colorbar range is chosen to highlight details below and above the bubbles. See *section S3* for numerical details.

133 tic approximation has been widely adopted by CRMs (Bryan & Fritsch, 2002; Khairoutdinov & Randall, 2003; Jung & Arakawa, 2008).

135 3.1 Anelastic response to buoyancy field

With vorticity and anelastic continuity equations, one can derive (see *SI section S1*)

$$\nabla_h^2 a + \frac{\partial}{\partial z} \left[\frac{1}{\rho_0} \frac{\partial}{\partial z} (\rho_0 a) \right] = \nabla_h^2 B + \mathcal{D}, \quad (1)$$

136 where $a \equiv \partial_t w$ is the vertical acceleration, B the buoyancy, and \mathcal{D} a quadratic function of spatial derivatives of velocity \mathbf{u} (i.e., associated with flow kinematics) that vanishes when $\mathbf{u} \equiv 0$. The influences of buoyancy and kinematics on a can thus be separately diagnosed. Here we focus on the response to buoyancy, which allows a direct contrast to conventional parameterizations.

141 In Eq. (1), the operator acting on a is elliptic, one thus expects a global response even for localized forcing (Houze, 1993). The response is accompanied by adjustment to horizontal convergence driven by locally hydrostatic pressure gradients (Jeevanjee & Romps, 2016) to ensure mass conservation. Note that buoyancy drives acceleration via $\nabla_h^2 B$ —flow evolves following horizontal variation of buoyancy.

146 To give a concrete sense of the nonlocal dynamics, Fig. 2 demonstrates two examples of the mass flux response $\rho_0 a$ (color shading) to idealized cylindrical buoyancy bubbles of 8-km diameter (magenta contours). Here a is from solving Eq. (1) (with $\mathcal{D} \equiv 0$)

149 for the two cases separately. The localized buoyancy generates strong upward acceler-
 150 ation within its diameter, accompanied by weak, broad downward acceleration in the sur-
 151 roundings. The extensive response reaches well below and above the bubble, driving a
 152 layer of flow into the convective region in the lower troposphere, as a consequence of grad-
 153 ually increasing $\rho_0 a$ with height, and outflow aloft from decreasing $\rho_0 a$. Other things equal,
 154 deeper bubbles generally result in greater response.

155 The nonlocal responses in Fig. 2 result from the elliptic operator in Eq. (1), and
 156 are well-known in principle (Cotton et al., 2010; Trapp, 2013). If the vertical velocity
 157 extends above the region where condensational heating can balance work against strat-
 158 ification (roughly the parcel-theory level of neutral buoyancy), a negative buoyancy ten-
 159 dency will occur. This results in the convective cold-top phenomenon (Holloway & Neelin,
 160 2007), with a region of negative buoyancy tending to cancel the response above, as il-
 161 lustrated on the right in Fig. 2. Here we focus on the properties of the nonlocal solution
 162 within and below the positively buoyant region. If this part of the updraft is saturated
 163 (above an unstratified boundary layer), latent heating tends to cancel negative buoyancy
 164 tendencies. Building on previous work, we can then ask under what conditions the non-
 165 local solutions might provide an explanation for the deep inflow, and what physics this
 166 suggests might be missing from parcel models.

167 3.2 Analytic vertical structures

For a more detailed characterization of the nonlocal dynamics, we apply a Fourier
 transform to Eq. (1)

$$-\frac{4\pi^2}{L^2}\hat{a} + \frac{\partial}{\partial z} \left[\frac{1}{\rho_0} \frac{\partial}{\partial z} (\rho_0 \hat{a}) \right] = -\frac{4\pi^2}{L^2}\hat{B}, \quad (2)$$

168 where $a \sim \hat{a}(z; k, \ell)e^{2\pi i(kx + \ell y)}$, $B \sim \hat{B}(z; k, \ell)e^{2\pi i(kx + \ell y)}$, and $L \equiv (k^2 + \ell^2)^{-1/2}$ is the
 169 horizontal wavelength.

Consider a simple buoyancy structure with $\hat{B}(z) \equiv \text{constant}$ within a layer and
 vanishing elsewhere—general profiles can be approximated by superposition. We can an-
 alytically solve Eq. (2) (*section S2*) for the homogeneous solutions

$$\hat{a}^\pm(z; k, \ell) \sim e^{\pm 2\pi z/L}, \quad (3)$$

and for the particular solution within the buoyant layer

$$\hat{a}^p(z; k, \ell) \approx \hat{B}(z; k, \ell). \quad (4)$$

170 The monochromatic (single-wavelength) solutions can then be constructed as a piece-
 171 wise linear combination of \hat{a}^\pm and \hat{a}^p by matching across layer boundaries, yielding so-
 172 lutions similar to Jeevanjee (2017). Each horizontal wavelength gives rise to a vertical
 173 e -folding scale $H_s \equiv L/2\pi$ —longer wavelength results in a greater range of nonlocal in-
 174 fluence.

175 Fig. 3a shows examples of \hat{a} (lines) given a buoyant layer of depth $H_B = 1$ km
 176 and $\hat{B} = 0.01$ m/s² (shadings) at various heights with $L = 5$ km. Above the buoy-
 177 ancy, the vanishing condition requires that $\hat{a} \sim e^{-2\pi z/L}$. Below the buoyancy for lay-
 178 ers away from the surface (compared with H_s), $\hat{a} \sim e^{+2\pi z/L}$, and the overall profiles
 179 appear to be symmetric in z with maximum occurring in the middle of the layers. But
 180 for a layer at low altitude, the surface boundary condition results in $\hat{a} \approx c_1 e^{+2\pi z/L} -$
 181 $c_2 e^{-2\pi z/L}$ —adding \hat{a}^p if the layer reaches the surface—causing an approximately linear
 182 dependence on height below the maximum as well as an overall weaker response mag-
 183 nitude. This surface control is generally important for sufficiently long wavelength (see
 184 also Fig. 3b, blue line).

185 To further illustrate how the layer depth and horizontal wavelength affect the so-
 186 lutions, Fig. 3b includes additional examples for a deeper layer of buoyancy ($H_B = 6$

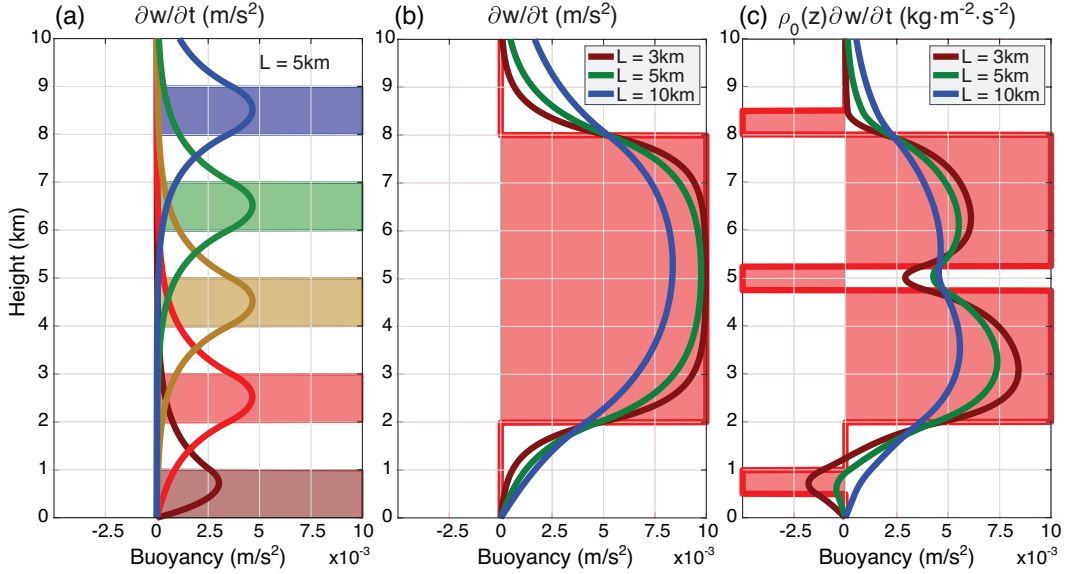


Figure 3. (a) Monochromatic solutions of vertical velocity response (lines) to individual buoyant layers located at different heights (shadings) with horizontal wavelength $L = 5$ km. (b) As in (a), for a deeper layer (red) and varying L . (c) As in (b), with additional thin layers of negative buoyancy, for vertical mass flux response. See *section S2* for numerical details.

187 km; red) and varying L . Short wavelength ($L/H_B \ll 1$) leads to limited nonlocal in-
 188 fluence, mostly confined in the vicinity of the layer boundaries (brown line). Conversely,
 189 long wavelength and/or relatively shallow layer ($L/H_B \gg 1$) would yield solutions ex-
 190 tending well outside the buoyant layer with reduced magnitude (blue line; also contrast
 191 with Fig. 3a). The aspect-ratio dependence is consistent with prior studies (Jeevanjee
 192 & Romps, 2016; Morrison, 2016), but for deep-inflow applications, L relative to a typi-
 193 cal distance from the surface is important. Note also that the inflow can also continue
 194 for a characteristic vertical scale $\sim H_s$ within the buoyant layer. The mass flux responses
 195 corresponding to the accelerations in Figs. 3a,b are similar but bottom-heavier since ρ_0
 196 decreases with height.

197 For a more sophisticated case, Fig. 3c shows the mass flux responses $\rho_0\hat{a}$ (lines) to
 198 an idealized deep-convective structure with the addition of (i) a near-surface convective
 199 inhibition (CIN) layer; (ii) a thin negatively-buoyant layer representing, e.g., effects of
 200 melting near freezing level; and (iii) a layer resembling the convective cold-top. For short
 201 wavelength, the response tracks the variation of buoyancy. But for sufficient horizontal
 202 scales, the solution due to net-positive buoyancy has no difficulty tunneling through verti-
 203 cally restricted layers of negative buoyancy or near-surface CIN layer. The cold-top used
 204 here is sufficient to limit the vertical extent of the updraft for the shortest wavelength,
 205 but would need to be more intense for the longer wavelengths.

206 This last observation—based on a monochromatic argument but also supported by
 207 the solutions in section 4—has practical implications. First, this helps understand why
 208 a nighttime CIN layer may not prevent pre-existing storms from moving into a region,
 209 e.g., over the Mississippi basin or the Amazon (Burleyson et al., 2016): the layer depth
 210 plus surface interactions limit the effect of CIN. This may also be relevant to elevated
 211 MCSs (Marshall et al., 2011). Second, it addresses a common issue in parcel computa-
 212 tions of convective available potential energy (CAPE) that have to contend with small
 213 layers in which parcel buoyancy goes negative (e.g., similar to the buoyancy in Fig. 3c)—

214 this can give rise to an underestimate of the energy actually available to convective storms;
 215 the results here indicate why updrafts in large storms easily penetrate such layers.

216 To briefly summarize the monochromatic dependence on scales: 1) the dependence
 217 is non-monotonic; the horizontal wavelength L determines the range of nonlocal verti-
 218 cal influence; small L yields the familiar limit of vertically localized response, while buoy-
 219 ancy layers that are thin compared to $L/2\pi$ yield response of limited magnitude. 2) L
 220 comparable to or exceeding a substantial fraction of the troposphere depth or of the height
 221 of the buoyant layer above the surface yields deep-inflow structure in the lower tropo-
 222 sphere.

223 4 Buoyancy Tartare—robustness to fine structures

224 Two important modifications occur as one moves from considering a single wave-
 225 length to more realistic cases. First, the buoyancy associated with convective updrafts
 226 tends to be localized. Features of a finite horizontal size D and net-positive buoyancy
 227 consist of Fourier component contributions from a broad range of wavelength, primar-
 228 ily $L \gtrsim D$ (*section S4*). This includes nonlocal effects beyond what one would antici-
 229 pate from the monochromatic considerations above, and is in contrast with prior stud-
 230 ies that emphasized the contribution from $L \approx D$ (Jeevanjee, 2017). Second, robust-
 231 ness to complex buoyancy structures associated with imperfectly mixed turbulent flow
 232 must be assessed.

233 To address this, we build net-positive buoyancy patches from an ensemble of smaller
 234 elements, using the shorthand “tartare” to describe these constructions of larger scale
 235 D from “minced” ingredients of size $d \ll D$. Figs. 4a,c display two such tartares of di-
 236 ameter $D \approx 10$ km consisting of warm (red) and cold (blue) bubbles of $d = 1$ km and
 237 depth 0.5 km. In the first set of examples (as in Fig. 4a) the tartares are constructed to
 238 illustrate the nonlocal influence below the buoyancy by placing them at a distance from
 239 the surface. The mean mass flux responses to 10 randomly generated tartares for each
 240 D are demonstrated in Fig. 4b (depth indicated by gray shading). Through interference,
 241 the integral of individual d -bubbles leads to primary Fourier contributions from $L \gtrsim D$
 242 for each D -tartare (*Fig. S1*). Thus for larger D or further below the buoyancy forcing,
 243 the responses converge towards linear dependence on height; see also Fig. 1b. For smaller
 244 D (e.g., $D \approx 5$ km) and closer to the forcing, the vertically localized behaviors—more
 245 rapid increase with height near the tartare base—from the smaller-scale $1 \lesssim L \lesssim 5$
 246 km Fourier components can be distinguished from the nonlocal, roughly-linear solutions
 247 at lower height ($z < 2.5$ km) that are dominated by contributions from $L \gtrsim 5$ km.

248 Figs. 4c,d offer additional examples for tilted tartares—to mimic storms under windshear—
 249 with a greater depth and lower base. The tilt does not greatly alter the nonlocal behav-
 250 ior for D exceeding a substantial fraction of the tropospheric depth. Since the tartare
 251 base is at $z = 2$ km, the responses appear roughly linear even for $D \approx 5$ km. In a more
 252 comprehensive setup where the evolution of buoyancy is included, the tilt impacts the
 253 location of rain, hence cooling by evaporation of raindrops relative to latent heating. Here,
 254 the point is simply that tilted convective systems are subject to the same nonlocal dy-
 255 namics.

256 Compared with idealized bubbles of the same dimensions and constant buoyancy
 257 (not shown), the tartare responses are weaker by a small fraction but otherwise exhibit
 258 similar profiles. This is consistent with the nonlocal dynamics being robust to small-scale
 259 variations and depending primarily on large-scale integral measures for the features of
 260 interest. The fine structures within the buoyant region give rise to localized intense ac-
 261 celerations. The effects of this on the horizontal average in Figs. 4b,d, may be seen in
 262 variations among instances of the tartare. Below the buoyant region, however, the non-
 263 local effects create relatively smooth structure even for individual instances. Furthermore,

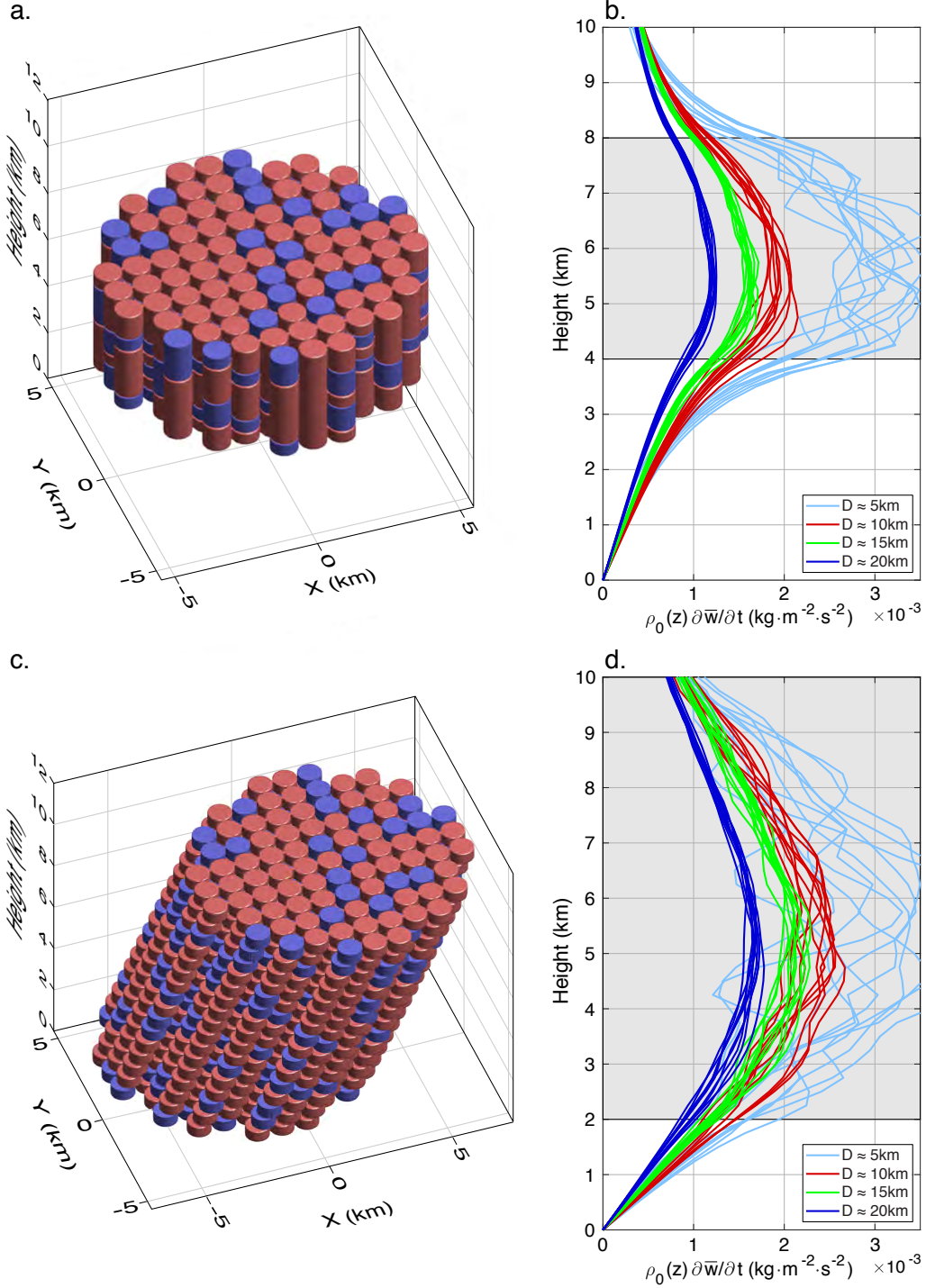


Figure 4. (a) A realization of a net-positive buoyancy tartare—an aggregate of stochastically-generated smaller positive (red) and negative (blue) buoyancy elements—of horizontal diameter $D \approx 10$ km and vertical extent $4 \leq z \leq 8$ km. Buoyancy value within individual element is approximately constant, and of equal strength for warm and cold elements. The ratio of numbers of warm to cold elements is set to 7:3. A ~ 12 km region of a 64-km domain is shown. (b) Theoretical response of convective mass flux to an ensemble of 10 tartare realizations as in (a), for varying D . The average buoyancy over each tartare is rescaled to $+0.01$ m/s². Each curve represents the mean profile within the tartare diameter. (c) As in (a), with vertical extent $2 \leq z \leq 10$ km and tilt $\approx 27^\circ$ ($\Delta z / \Delta x \equiv 2$). (d) As in (b), but for vertically tilted tartares as in (c). See *section S3* for numerical details.

264 this horizontal-average mass flux is equivalent to the horizontal convergence of air en-
 265 tering the feature, bringing in unmodified air from the far field and thus tending to dom-
 266 inate the effect of the environment on the feature.

267 5 Discussion

268 Aspects of nonhydrostatic nonlocal solutions have been studied in recent years with
 269 different focuses. For instance, the rate of entrainment of individual updrafts as a func-
 270 tion of updraft size has been examined for dry plumes (Lecoanet & Jeevanjee, 2019). Re-
 271 lationships of entrainment and plume scale have been incorporated into recent convec-
 272 tive parameterizations for preliminary testing (Peters et al., 2021). Such approaches are
 273 similar to modifying the idealized monochromatic response as in Fig. 3 as building blocks
 274 for constraining mass flux profiles. Although results here are aimed at explaining a fea-
 275 ture of observations, they have implications for such parameterization efforts. In par-
 276 ticular, they underline that the leading-order flow response to a buoyant region of a fi-
 277 nite size includes contributions from a range of wavelengths. This is key to the robust-
 278 ness of nonlocal dynamics at the larger scales involved in convection—those less amenable
 279 to treatment by moment closures or traditional turbulent assumptions—especially when
 280 one has in mind the formulation for organized ensembles of smaller structures (Moncrieff
 281 et al., 2017). Superparameterizations include representations of all these effects by par-
 282 tially resolving them with CRMs embedded into GCM grid-boxes (Chern et al., 2016;
 283 Jansson et al., 2019; Jones et al., 2019). The nonlocal effects whose importance is em-
 284 phasized here are thus likely captured, even if small-scale turbulence is not resolved—
 285 but superparameterization remains computationally expensive. Approaches such as Morrison
 286 (2017) and Lecoanet and Jeevanjee (2019) may be promising if generalized to include
 287 the nonlocal effects underlined here both vertically and horizontally. Overall, leverag-
 288 ing anelastic solutions such as those here can help move parameterizations away from
 289 the idealization of entrainment as determined purely locally by a single parameter.

290 In light of these results, what can be considered universal regarding the convective
 291 mass flux profile? Not so much a specific profile shape, but the inherent vertically and
 292 horizontally nonlocal effects tending to yield a deep contribution to the mass flux. The
 293 nonlocal dynamics is effective at integrating over heterogeneous buoyancy (as in the tartare
 294 solutions), and can generate deep inflow robustly under a wide range of conditions. Vari-
 295 ations in the distribution of buoyancy can create departures from this. In particular, a
 296 layer of negative buoyancy can yield reductions in the vertical increase of mass flux, or
 297 even a low-level layer of negative vertical velocity at small scales. Yet because the non-
 298 local dynamics operates persistently, deep-inflow profiles tend to appear in averages of
 299 mass flux over many convective instances.

300 The observationally motivated hypothesis that there is a common explanation for
 301 the deep inflow into heavily precipitating unorganized convection and mesoscale-organized
 302 convection indeed has a simple explanation: the nonlocal dynamics entailing interaction
 303 between the buoyant layer and the surface. The robustness of this effect, especially at
 304 scales relevant for both large cumulonimbus and MCSs, supports the potential for pa-
 305 rameterizing aspects of these systems. Although it implies the need to include nonlocal,
 306 anelastic dynamics in convective parameterizations, the overall effect is to simplify key
 307 aspects of the interaction with the thermodynamic environment for large convective en-
 308 tities.

309 Appendix A Convective precipitation feature scales and MCS iden- 310 tification

311 For convective precipitation features, we use the TRMM 2A25 data (TRMM, 2011)
 312 for the period of June 2002 through May 2014 that include PR retrievals of surface rain
 313 rate (*rain*) and type (*rainType*) at $5 \text{ km} \times 5 \text{ km}$ resolution covering 40°S - 40°N . The

314 values of *rainType* consist of three numerical digits, and here we consider 2X0 (X = 0,
 315 2, 3, 4) convective. Note that these are different from shallow-convective and have $rain \geq$
 316 0.11 mm/h—the minimum detectable by the PR. For each 2A25 file (i.e., one orbit) we
 317 identify all contiguous areas and/or along-track chords consisting of convective raining
 318 pixels for the two measures of convective feature size. We further associate each area/chord
 319 with MCS or non-MCS depending on whether the feature overlaps with an MCS iden-
 320 tified following Mohr and Zipser (1996) for simple criteria not directly dependent on pre-
 321 cipitation: With the 10.8 μm brightness temperature (T_{B11}) from the Merged IR prod-
 322 uct (Janowiak et al., 2017), for each IR snapshot, we identify MCS as an area with $T_{B11} <$
 323 250 K of at least 2,000 km^2 and an enclosed minimum < 225 K.

324 Acknowledgments

325 This work was supported by National Science Foundation grant AGS-1936810 and National
 326 Oceanic and Atmospheric Administration grant NA21OAR4310354. We thank J.
 327 Meyerson for graphical assistance.

328 Data availability statement

329 The TRMM 2A25 (TRMM, 2011) and Merged IR products (Janowiak et al., 2017)
 330 are maintained and provided by NASA’s GES DISC publicly accessible via [https://](https://disc.gsfc.nasa.gov/)
 331 disc.gsfc.nasa.gov/.

332 References

- 333 Ahmed, F., & Neelin, J. D. (2018). Reverse engineering the tropical precipitation-
 334 buoyancy relationship. *Journal of the Atmospheric Sciences*, *75*, 1587–
 335 1608. Retrieved from [http://journals.ametsoc.org/doi/10.1175/](http://journals.ametsoc.org/doi/10.1175/JAS-D-17-0333.1)
 336 [JAS-D-17-0333.1](http://journals.ametsoc.org/doi/10.1175/JAS-D-17-0333.1) doi: 10.1175/JAS-D-17-0333.1
- 337 Arakawa, A., & Schubert, W. H. (1974). Interaction of a cumulus cloud ensemble
 338 with the large-scale environment, Part I. *Journal of Atmospheric Sciences*,
 339 *31*(3), 674–701.
- 340 Bretherton, C. S., Henn, B., Kwa, A., Brenowitz, N. D., Watt-Meyer, O., McGib-
 341 bon, J., ... Harris, L. (2021). Correcting coarse-grid weather and climate
 342 models by machine learning from global storm-resolving simulations. *Preprint*
 343 *on https://www.essoar.org/*.
- 344 Bryan, G. H., & Fritsch, J. M. (2002). A benchmark simulation for moist nonhydro-
 345 static numerical models. *Monthly Weather Review*, *130*(12), 2917–2928.
- 346 Burleyson, C. D., Feng, Z., Hagos, S. M., Fast, J., Machado, L. A., & Martin, S. T.
 347 (2016). Spatial variability of the background diurnal cycle of deep convec-
 348 tion around the GoAmazon2014/5 field campaign sites. *Journal of Applied*
 349 *Meteorology and Climatology*, *55*(7), 1579–1598.
- 350 Chern, J.-D., Tao, W.-K., Lang, S. E., Matsui, T., Li, J.-L., Mohr, K. I., ... Peters-
 351 Lidard, C. D. (2016). Performance of the Goddard multiscale modeling
 352 framework with Goddard ice microphysical schemes. *Journal of Advances in*
 353 *Modeling Earth Systems*, *8*(1), 66–95.
- 354 Cotton, W. R., Bryan, G. H., & Van den Heever, S. C. (2010). *Storm and cloud dy-*
 355 *namics*. Academic press.
- 356 Del Genio, A. D., & Wu, J. (2010). The role of entrainment in the diurnal cycle of
 357 continental convection. *Journal of Climate*, *23*(10), 2722–2738.
- 358 de Rooy, W. C., & Siebesma, A. P. (2010). Analytical expressions for entrainment
 359 and detrainment in cumulus convection. *Quart. J. R. Meteorol. Soc.*, *136*,
 360 1216–1227. doi: 10.1002/qj.640
- 361 Ferrier, B. S., & Houze, R. A. (1989). One-dimensional time-dependent modeling of
 362 GATE cumulonimbus convection. *J. Atmos. Sci.*, *46*, 330–352.

- 363 Holloway, C. E., & Neelin, J. D. (2007). The convective cold top and quasi equilib-
 364 rium. *Journal of the atmospheric sciences*, *64*(5), 1467–1487.
- 365 Houghton, H. G., & Cramer, H. E. (1951). A theory of entrainment in convective
 366 currents. *Journal of Atmospheric Sciences*, *8*(2), 95–102.
- 367 Houze, R. A. (1993). *Cloud Dynamics*. Academic Press.
- 368 Janowiak, J., Joyce, B., & Xie, P. (2017). *NCEP/CPC L3 Half Hourly 4km Global*
 369 *(60S - 60N) Merged IR V1*. Edited by Andrey Savtchenko, Greenbelt, MD,
 370 Goddard Earth Sciences Data and Information Services Center. (Accessed
 371 7-Jan-2020) doi: 10.5067/P4HZB9N27EKU
- 372 Jansson, F., van den Oord, G., Pelupessy, I., Grönqvist, J. H., Siebesma, A. P., &
 373 Crommelin, D. (2019). Regional superparameterization in a global circulation
 374 model using large eddy simulations. *Journal of Advances in Modeling Earth*
 375 *Systems*, *11*(9), 2958–2979.
- 376 Jeevanjee, N. (2017). Vertical velocity in the gray zone. *Journal of Advances in*
 377 *Modeling Earth Systems*, *9*(6), 2304–2316.
- 378 Jeevanjee, N., & Romps, D. M. (2016). Effective buoyancy at the surface and aloft.
 379 *Quarterly Journal of the Royal Meteorological Society*, *142*(695), 811–820.
- 380 Jones, T. R., Randall, D. A., & Branson, M. D. (2019). Multiple-instance superpa-
 381 rameterization: 1. Concept, and predictability of precipitation. *Journal of Ad-*
 382 *vances in Modeling Earth Systems*, *11*(11), 3497–3520.
- 383 Jung, J.-H., & Arakawa, A. (2008). A three-dimensional anelastic model based on
 384 the vorticity equation. *Monthly weather review*, *136*(1), 276–294.
- 385 Khairoutdinov, M. F., & Randall, D. A. (2003). Cloud resolving modeling of the
 386 arm summer 1997 IOP: Model formulation, results, uncertainties, and sensitivi-
 387 ties. *Journal of Atmospheric Sciences*, *60*(4), 607–625.
- 388 Kuang, Z., & Bretherton, C. S. (2006). A mass-flux scheme view of a high-resolution
 389 simulation of a transition from shallow to deep cumulus convection. *J. Atmos.*
 390 *Sci.*, *63*, 1895–1909.
- 391 Kuo, Y.-H., Neelin, J. D., Booth, J. F., Chen, C.-C., Chen, W.-T., Gettelman, A.,
 392 ... Zhao, M. (2020). Convective transition statistics over tropical oceans for
 393 climate model diagnostics: GCM evaluation. *J. Atmos. Sci.*, *77*, 379–403. doi:
 394 10.1175/JAS-D-19-0132.1
- 395 Lecoanet, D., & Jeevanjee, N. (2019). Entrainment in resolved, dry thermals. *Jour-*
 396 *nal of the Atmospheric Sciences*, *76*(12), 3785–3801.
- 397 LeMone, M. A., & Zipser, E. J. (1980). Cumulonimbus vertical velocity events in
 398 GATE. Part I: Diameter, intensity and mass flux. *Journal of Atmospheric Sci-*
 399 *ences*, *37*(11), 2444–2457.
- 400 Leung, L. R., Boos, W. R., Catto, J. L., DeMott, C., Martin, G. M., Neelin, J. D.,
 401 ... others (2022). Exploratory precipitation metrics: spatiotemporal character-
 402 istics, process-oriented, and phenomena-based. *Journal of Climate*, 1–55.
- 403 Li, Y., Zipser, E. J., Krueger, S. K., & Zulauf, M. A. (2008). Cloud-resolving mod-
 404 eling of deep convection during KWAJEX. Part I: Comparison to TRMM
 405 satellite and ground-based radar observations. *Monthly weather review*, *136*(7),
 406 2699–2712.
- 407 Lucas, C., Zipser, E. J., & Lemone, M. A. (1994). Vertical velocity in oceanic con-
 408 vection off tropical Australia. *Journal of Atmospheric sciences*, *51*(21), 3183–
 409 3193.
- 410 Markowski, P., & Richardson, Y. (2011). *Mesoscale meteorology in midlatitudes*
 411 (Vol. 2). John Wiley & Sons.
- 412 Marsham, J. H., Trier, S. B., Weckwerth, T. M., & Wilson, J. W. (2011). Obser-
 413 vations of elevated convection initiation leading to a surface-based squall line
 414 during 13 June IHOP 2002. *Monthly Weather Review*, *139*(1), 247–271.
- 415 Masunaga, H., & Luo, Z. J. (2016). Convective and large-scale mass flux profiles
 416 over tropical oceans determined from synergistic analysis of a suite of satel-
 417 lite observations. *Journal of Geophysical Research: Atmospheres*, *121*(13),

- 418 7958–7974.
- 419 Mohr, K. I., & Zipser, E. J. (1996). Mesoscale convective systems defined by their
420 85-GHz ice scattering signature: Size and intensity comparison over tropical
421 oceans and continents. *Mon. Wea. Rev.*, *124*, 2417–2437.
- 422 Moncrieff, M. W. (1992). Organized convective systems: Archetypal dynamical mod-
423 els, mass and momentum flux theory, and parametrization. *Quarterly Journal*
424 *of the Royal Meteorological Society*, *118*(507), 819–850.
- 425 Moncrieff, M. W., Liu, C., & Bogenschutz, P. (2017). Simulation, modeling, and
426 dynamically based parameterization of organized tropical convection for global
427 climate models. *Journal of the Atmospheric Sciences*, *74*(5), 1363–1380.
- 428 Moncrieff, M. W., Waliser, D. E., Miller, M. J., Shapiro, M. A., Asrar, G. R., &
429 Caughey, J. (2012). Multiscale convective organization and the yote virtual
430 global field campaign. *Bulletin of the American Meteorological Society*, *93*(8),
431 1171–1187.
- 432 Morrison, H. (2016). Impacts of updraft size and dimensionality on the perturbation
433 pressure and vertical velocity in cumulus convection. Part II: Comparison of
434 theoretical and numerical solutions and fully dynamical simulations. *Journal of*
435 *the Atmospheric Sciences*, *73*(4), 1455–1480.
- 436 Morrison, H. (2017). An analytic description of the structure and evolution of grow-
437 ing deep cumulus updrafts. *Journal of the Atmospheric Sciences*, *74*(3), 809–
438 834.
- 439 Nesbitt, S., Cifelli, W. R., & Rutledge, S. A. (2006). Storm morphology and rainfall
440 characteristics of TRMM precipitation features. *Mon. Wea. Rev.*, *134*, 2702–
441 2721.
- 442 Ogura, Y., & Phillips, N. A. (1962). Scale analysis of deep and shallow convection in
443 the atmosphere. *J. atmos. Sci.*, *19*(2), 173–179.
- 444 Peters, J., Morrison, H., Zhang, G., & Powell, S. (2021). Improving the physical ba-
445 sis for updraft dynamics in deep convection parameterizations. *Journal of Ad-*
446 *vances in Modeling Earth Systems*, *13*(2), e2020MS002282.
- 447 Plant, R. (2010). A review of the theoretical basis for bulk mass flux convective pa-
448 rameterization. *Atmospheric Chemistry and Physics*, *10*(8), 3529–3544.
- 449 Randall, D., Khairoutdinov, M., Arakawa, A., & Grabowski, W. (2003). Breaking
450 the cloud parameterization deadlock. *Bulletin of the American Meteorological*
451 *Society*, *84*(11), 1547–1564.
- 452 Robe, F. R., & Emanuel, K. A. (1996). Moist convective scaling: Some inferences
453 from three-dimensional cloud ensemble simulations. *J. Atmos. Sci.*, *53*, 3265–
454 3275.
- 455 Romps, D. M. (2010). A direct measure of entrainment. *Journal of the Atmospheric*
456 *Sciences*, *67*(6), 1908–1927.
- 457 Savazzi, A. C., Jakob, C., & Siebesma, A. P. (2021). Convective mass-flux from
458 long term radar reflectivities over Darwin, Australia. *Journal of Geophysical*
459 *Research: Atmospheres*, e2021JD034910.
- 460 Schiro, K. A., Ahmed, F., Giangrande, S. E., & Neelin, J. D. (2018). GoAma-
461 zon2014/5 campaign points to deep-inflow approach to deep convection across
462 scales. *Proceedings of the National Academy of Sciences*, *115*(18), 4577–4582.
- 463 Sherwood, S. C., Bony, S., & Dufresne, J.-L. (2014). Spread in model climate sensi-
464 tivity traced to atmospheric convective mixing. *Nature*, *505*(7481), 37.
- 465 Siebesma, A. P., Bretherton, C. S., Brown, A., Chlond, A., Cuxart, J., Duynkerke,
466 P. G., ... others (2003). A large eddy simulation intercomparison study of
467 shallow cumulus convection. *Journal of the Atmospheric Sciences*, *60*(10),
468 1201–1219.
- 469 Siebesma, A. P., Soares, P. M. M., & Teixeira, J. (2007). A combined eddy diffusiv-
470 ity mass flux approach for the convective boundary layer. *J. Atmos. Sci.*, *64*,
471 1230–1248.

- 472 Trapp, R. J. (2013). *Mesoscale-convective processes in the atmosphere*. Cambridge
473 University Press.
- 474 TRMM. (2011). *TRMM Precipitation Radar rainfall rate and profile L2 1.5*
475 *hours V7*. Goddard Earth Sciences Data and Information Services Cen-
476 ter. (Accessed 19-Aug-2016) doi: [https://disc.gsfc.nasa.gov/datacollection/](https://disc.gsfc.nasa.gov/datacollection/TRMM_2A25_7.html)
477 [TRMM_2A25_7.html](https://disc.gsfc.nasa.gov/datacollection/TRMM_2A25_7.html)
- 478 Wing, A. A., Stauffer, C. L., Becker, T., Reed, K. A., Ahn, M.-S., Arnold, N. P.,
479 ... others (2020). Clouds and convective self-aggregation in a multimodel
480 ensemble of radiative-convective equilibrium simulations. *Journal of advances*
481 *in modeling earth systems*, *12*(9), e2020MS002138.
- 482 Yano, J.-I., & Moncrieff, M. W. (2016). Numerical archetypal parameterization
483 for mesoscale convective systems. *Journal of the Atmospheric Sciences*, *73*(7),
484 2585–2602.

Supplementary Information for

Conditions for convective deep inflow

Yi-Hung Kuo & J. David Neelin

Yi-Hung Kuo

E-mail: yhkuo@atmos.ucla.edu

This PDF file includes:

Supplementary sections S1–S4

Fig. S1

Supporting Information Text

S1. Governing equation for response

In the main text, the nonlocal dynamics is studied via diagnosing the vertical acceleration in response to buoyancy using Eq. (1). Here we demonstrate how the equation can be derived from the vorticity and anelastic continuity equations.

Notations and constants. The 3D velocity and vorticity are denoted by $\mathbf{u} = (\mathbf{u}_h, w) = (u, v, w)$ and $\boldsymbol{\omega} \equiv \nabla \times \mathbf{u} = (\xi, \eta, \zeta)$, respectively (subscript h for horizontal components). We use ρ and θ for atmospheric density and potential temperature, and subscript 0 for hydrostatic reference states that are time-invariant and horizontally homogeneous. Relevant constants for dry air used here include the gas constant $R_d = 287$ J/kg/K, specific heat at constant pressure $c_{pd} = 1,005$ J/kg/K and at constant volume $c_{vd} = 718$ J/kg/K (Houze, 1993). Also, $g = 9.81$ m/s².

Derivation. Following Jung and Arakawa (2008), from the definition of $\boldsymbol{\omega}$,

$$\begin{aligned} \partial_y \xi - \partial_x \eta &\equiv \nabla_h^2 w - \partial_z (\nabla_h \cdot \mathbf{u}_h) \\ &= \nabla_h^2 w + \partial_z \left[\frac{1}{\rho_0} \partial_z (\rho_0 w) \right]. \end{aligned} \quad (\text{S1})$$

The last equality follows the anelastic continuity equation

$$\nabla_h \cdot (\rho_0 \mathbf{u}_h) + \partial_z (\rho_0 w) = 0.$$

Applying ∂_t to both sides of Eq. (S1) and substituting $\partial_t \xi$, $\partial_t \eta$ using the vorticity equation, it is straightforward to derive Eq. (1) with

$$\begin{aligned} B &\equiv g \left(\frac{\theta'}{\theta_0} + 0.61q_v - q_c \right), \\ \mathcal{D} &\equiv -\frac{\partial}{\partial z} \nabla \cdot [\mathbf{u} \times (\boldsymbol{\omega} + \mathbf{f})] + \nabla^2 (u\eta - v\xi), \end{aligned}$$

where B is the buoyancy, θ' the potential temperature deviation from θ_0 , q_v and q_c the mixing ratios of water vapor and condensate, \mathbf{f} the Coriolis parameter pointing along the z -direction. Note that $(u\eta - v\xi)$ is the z -component of $\mathbf{u} \times \boldsymbol{\omega}$. It should also be noted that Eq. (1) is similar to the decomposition adopted by Jeevanjee and Romps (2016) in that both capture the nonlocal nature and have the identical response to buoyancy. \mathcal{D} can become a significant modifier in strong flow regimes, but spatial filtering by the nonlocal solutions to Eq. (1) would in principle apply to forcing by \mathcal{D} as well.

Atmospheric density. In practice, $\rho_0(z)$ is often determined by a prescribed reference potential temperature $\theta_0(z)$ assuming hydrostatic balance. For the current study, to facilitate our analytic approach, we assume

$$\rho_0(z) \equiv \frac{P_0}{R_d \Theta_0} \left(1 - \frac{z}{H} \right)^\beta,$$

with the reference pressure P_0 and potential temperature Θ_0 at $z = 0$ (values set to 1,000 hPa and 292.8 K so that $H \equiv c_{pd} \Theta_0 / g \equiv 30$ km throughout this study), and $\beta = c_{vd} / R_d \approx 2.5$ for an isentropic atmosphere (i.e., $\theta_0 \equiv \Theta_0$). Note that the atmospheric stability can be adjusted by slightly varying β , which will not alter our key findings, and neither will a more general ρ_0 .

S2. Analytic solutions

In section 3.2 of the main text, it was stated that the monochromatic (i.e., single horizontal wavelength) vertical structure of the response can be solved analytically for individual Fourier modes. To do so, we introduce the changes of variables

$$s \equiv 1 - \frac{z}{H}, \quad A(s) \equiv \sqrt{\rho_0} \hat{a}, \quad (\text{S2})$$

with which Eq. (2) becomes

$$A'' - \lambda(s)^2 A = -F(s). \quad (\text{S3})$$

Here $(\cdot)'$ denotes d/ds , and

$$\begin{aligned} F(s) &\equiv \lambda_0^2 \sqrt{\rho_0} \hat{B}, \\ \lambda(s) &\equiv \lambda_0 \left(1 + \frac{\gamma}{\lambda_0^2 s^2} \right)^{1/2}, \\ \lambda_0 &\equiv 2\pi H / L, \\ \gamma &\equiv \frac{\beta}{2} \left(\frac{\beta}{2} + 1 \right). \end{aligned}$$

A WKB approach gives approximate homogeneous solutions to Eq. (S3)

$$A^\pm(s) = e^{\mp\lambda(s)s} \left(\frac{\lambda(s)s - \sqrt{\gamma}}{\lambda(s)s + \sqrt{\gamma}} \right)^{\mp\sqrt{\gamma}/2} \lambda(s)^{-1/2}, \quad (\text{S4})$$

leading to $\widehat{a}^\pm(z)$ in Eq. (3). When \widehat{B} is slowly-varying, such that $O(F''/\lambda^2) \ll O(F)$, this condition allows an asymptotic approximation to the particular solution

$$A^p(s) = \frac{1}{\lambda(s)^2} \left[F(s) + \frac{F''(s)}{\lambda(s)^2} \right], \quad (\text{S5})$$

leading to $\widehat{a}^p(z)$ in Eq. (4).

The monochromatic solutions in Fig. 3 are evaluated using Eqs. (S4) and (S5). The value and first derivative of the solutions are matched across the jumps of buoyancy in the vertical. This requires inverting regular yet ill-conditioned (because of the exponentials) linear systems for which symbolic computations are employed.

The monochromatic responses to a single layer of buoyancy at various height and for different horizontal wavelength L form a basis that is used for building responses to more general buoyancy configurations in Fig. 4. The solutions built this way are consistent with those obtained by numerically solving Eq. (1).

For general ρ_0 , Eqs. (S2) and (S3) still apply though with different $\lambda(s)$ and approximate solutions.

S3. Numerical evaluations of responses

This section provides additional details for the computations of the solutions presented in Figs. 1b, 2 and 4 in the main text.

To construct the idealized buoyancy bubbles, we use the normal cumulative distribution function denoted by

$$\mathcal{N}(\tau, \tau_0, \sigma) \equiv \frac{1}{2} \operatorname{erfc}\left(-\frac{\tau - \tau_0}{\sqrt{2}\sigma}\right).$$

In Fig. 2, the cylindrical bubbles of positive buoyancy (units: m/s^2) are given by

$$B_+(r, z) \equiv 10^{-2} \times [1 - \mathcal{N}(r, 4, 0.2)]\mathcal{N}(z, 4, 0.1)[1 - \mathcal{N}(z, 8, 0.1)],$$

where $r \equiv \sqrt{x^2 + y^2}$. Both r and z are in km. The bubbles have a horizontal diameter of 8 km, and extend vertically from 4 to 8 km (magenta contours). The negatively buoyant bubble (blue contour) resembling convective cold-top is given by

$$B_-(r, z) \equiv -6 \cdot 10^{-2} \times [1 - \mathcal{N}(r, 4, 1.2)]\mathcal{N}(z, 8.2, 0.1)[1 - \mathcal{N}(z, 8.5, 0.1)].$$

The cold-top has the same diameter (but a more moderate transition) in the horizontal, a narrower vertical extent from 8.2 to 8.5 km, and a greater magnitude of buoyancy. For the two cases displayed in Fig. 2, instead of directly solving Eq. (1), we consider a domain doubly periodic in the horizontal $-16 \leq x, y \leq 16$ km, and separately solve Eq. (2) for $\widehat{a}(z; k, \ell)$ numerically with vanishing conditions at $z = 0, 20$ km for all admissible (k, ℓ) , then reconstruct a via inverse Fourier transform. The horizontal and vertical grid spacings used are 125 and 6 m.

The tartares in Fig. 4 consist of raw elements having buoyancy of the form

$$b_\pm \equiv \pm \frac{1}{2} \operatorname{erfc}\left(\frac{r - 0.5}{0.02}\right) \mathcal{H}(z - z_B)\mathcal{H}(z_B + 0.5 - z),$$

with r, z, z_B in km, and \mathcal{H} denoting the Heaviside function. When building a tartare of diameter $\approx D$, the \pm signs are randomly assigned with 7 : 3 probabilities. Then the integral buoyancy of each tartare is rescaled to that of $10^{-2} \times \frac{1}{2} \operatorname{erfc}\left(\frac{r-D/2}{0.2}\right) \times \mathcal{H}(z - z_B)\mathcal{H}(z_T - z)$ ($\approx 0.01 \text{ m/s}^2$ on average within the tartare of diameter D and depth $z_T - z_B$). The overall responses to buoyancy tartares are computed utilizing the monochromatic basis in a 64 km \times 64 km doubly-periodic horizontal domain with grid spacing 62.5 m. Using the analytic expressions for vertical structures (as described in section S2), the accuracy of solutions is not affected by vertical grid spacing. For tilted tartares, the tartare cross section for $5.5 \leq z \leq 6$ km is centered at $x = y = 0$. The profiles in Figs. 4b,d represent the mass flux responses averaged over $x^2 + y^2 \leq D/2$ for individual tartare realizations. The mean profiles averaged over an ensemble of 10 tartare realizations (as shown in Fig. 4b) for varying diameter D are summarized in Fig. 1b for the lower troposphere.

S4. Horizontal features of finite size and their Fourier spectrum

In section 4 of the main text, we noted the importance of the fact that net-positive buoyancy features of a finite horizontal size D consist of Fourier component contributions primarily from wavelength $L \gtrsim D$. Here we provide an analytic illustration of this and numerical examples for more realistic instances.

Analytic illustration. Consider an idealized feature of size D in a large 1D domain

$$B_H(x) \equiv \begin{cases} 1, & |x| \leq D/2, \\ 0, & \text{elsewhere,} \end{cases}$$

and its Fourier coefficient (omitting the normalization factor that varies with domain size)

$$\widehat{B}_H(k) \equiv \int B_H(x) e^{-2\pi i k x} dx.$$

When $L \equiv 1/|k|$ is comparable to or smaller than D , the sign of the integrand changes. The positive and negative contributions to the integral tend to cancel, resulting in $\widehat{B}_H(k)$ of small magnitude. In contrast, when L exceeds D (or $2D$ to be conservative), the integrand tends to be of the same sign, leading to a substantial $\widehat{B}_H(k)$.

For this idealized case, the integral can be readily evaluated

$$\widehat{B}_H(k) = \begin{cases} \frac{D}{k\pi D} \sin(k\pi D), & k \neq 0, \\ D, & k = 0. \end{cases}$$

Normalize \widehat{B}_H by its value at $k = 0$. The magnitude of \widehat{B}_H is bounded by the envelope $1/|k|\pi D \equiv L/\pi D$, i.e., there are important contributions from all Fourier components of wavelength on the order of or larger than D . Assuming a single dominant wavelength at D can thus be highly misleading, especially for aspects where dynamics favors the longer wavelengths in the response.

More realistic illustration. In 2D, consider the idealized pattern

$$b_H(x, y) \equiv \frac{1}{2} \operatorname{erfc} \left(\frac{r - 0.5}{0.02} \right),$$

where $r \equiv \sqrt{x^2 + y^2}$ (units: km). $b_H \approx 1$ for $r < 0.5$ km and vanishes elsewhere with a smooth transition over a width ~ 0.06 km. In Fig. S1, the pattern of b_h and its Fourier coefficient

$$\widehat{b}_H(k, \ell) \equiv \iint b_H(x, y) e^{-2\pi i(kx + \ell y)} dx dy$$

are represented by gray lines. b_h has its primary Fourier contribution from $K \equiv \sqrt{k^2 + \ell^2} \lesssim 1$ (km^{-1}), or $L \equiv 1/K \gtrsim 1$ km.

Using b_h , we construct more complicated net-positive patterns as

$$B_H(x, y) \equiv \sum_{n=1}^{1,000} s_n m_n b_H(x - x_n, y - y_n),$$

where $s_n = \pm 1$ with 7:3 positive-to-negative ratio, m_n the magnitude uniformly distributed in $[0, 1]$, and (x_n, y_n) the center of b_h uniformly spread within a circle of diameter 10 km. Figure S1a shows one such realization, which seems plausible for convection. Its Fourier coefficient for $k \geq 0, \ell = 0$ is included in Fig. S1b (magenta thick) together with the results for nine more realizations. These examples demonstrate that when an ensemble of 1-km patterns form net-positive features of larger scale (here diameter 10 km), the primary Fourier contributions are from $K \lesssim 1/10$ (km^{-1}), or $L \gtrsim 10$ km.

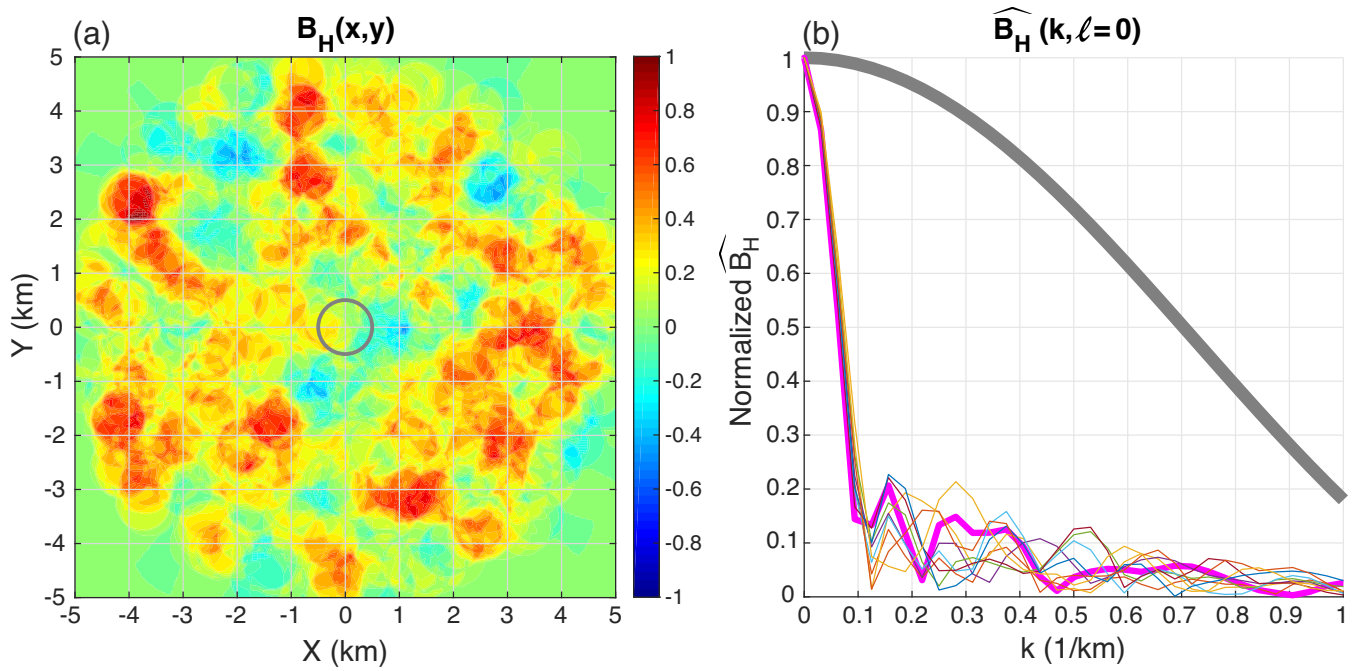


Fig. S1. (a) An idealized buoyancy pattern b_h of diameter 1 km (gray contour) and a realization of a stochastically-generated net-positive pattern of diameter ≈ 10 km (color shading) shown on a $10 \text{ km} \times 10 \text{ km}$ zoom of a $32 \text{ km} \times 32 \text{ km}$ doubly-periodic domain. The pattern is constructed using 1,000 copies of b_h , with their centers randomly spread within a circle of diameter 10 km, magnitudes uniformly distributed in $[0, 1]$, and 7:3 positive-to-negative sign ratio. (b) The Fourier coefficients of b_h (gray thick) and 10 realizations of the stochastically-generated net-positive patterns (colors) for wavenumbers $k \geq 0, \ell = 0$. The Fourier coefficient of the pattern in (a) is indicated by the thick magenta line. The Fourier coefficients are normalized by their values at $k = \ell = 0$.